

# **HiSST: 4th International Conference on High-Speed Vehicle Science Technology**

22-26 September 2025, Tours, France



## Numerical study of the laminar-turbulent transition on a hypersonic vehicle in flight and wind tunnel conditions

Selwyn Van der Laan 1, Mathieu Lugrin 2, Clément Caillaud 3, Cédric Content 4, Denis Sipp 5

## **Abstract**

A numerical study analyzes boundary layer stability over a Cone-Cylinder-Flare (CCF) geometry at Mach 6 and Reynolds number  $Re = 4.62 \times 10^6 \ [m^{-1}]$ , focusing on the impact of wall-to-recovery temperature similarity on hypersonic transition. Three cases are compared: typical cold-wall flight, standard wind tunnel conditions, and a third case with enhanced wall cooling to match flight similarity parameters. Global stability and resolvent analyses reveal that wall cooling and higher stagnation temperatures significantly destabilize global modes. While both first and second Mack modes are active in tunnel tests, only the second mode dominates in flight. The third case, with temperature similarity, successfully replicates flight transition mechanisms despite lower stagnation temperatures. These results highlight the crucial role of wall-to-recovery temperature in accurately modeling hypersonic transition and the limitations of conventional ground testing.

Keywords: Hypersonic, Transition, Stability

#### **Nomenclature**

Latin

M – Mach number

Re – Unit Reynolds number  $[m^{-1}]$ 

T – Temperature [K]

 $T_r$  – Recovery temperature [K]

P – Pressure [ $P\alpha$ ]

St – Strouhal number

f – frequency [kHz]

*m* – Azimuthal frequency

*q* – State vector

u – Streamwise velocity [ $m.s^{-1}$ ]

 $\mathcal{J}$  – Jacobian

 $\mathcal{N}$  – Navier-Stokes Operator

 $\mathcal{R}$  – Resolvent Operator

Greek

 $\rho$  – Density [ $kg.m^{-3}$ ]

 $\omega$  – Angular frequency [ $rad.s^{-1}$ ]

 $\delta$  – Boundary layer thickness [mm]

 $\eta$  – Wall normal distance [mm]

 $\sigma$  – Growth rate

 $\mu$  – Energy gain

Superscripts

- Baseflow quantities

√ – Perturbed quantities

Subscripts

·e – Boundary layer edge values

 $\cdot_{\infty}$  – Freestream values

⋅<sub>0</sub> – Stagnation values

·w - Wall values

## 1. Introduction

Transition to turbulence in hypersonic boundary layers remains a complex and not fully understood phenomenon, posing major challenges for the safe and efficient design of hypersonic vehicles. A key engineering consequence is the design of Thermal Protection Systems (TPS), which shield vehicles from severe aerodynamic heating. Turbulent boundary layers can generate heat fluxes up to three times higher than laminar ones, while transitional phases may produce localized peaks exceeding turbulent levels [1]. Errors in predicting transition location or mechanism may lead to either overly conservative TPS, adding

<sup>&</sup>lt;sup>1</sup>DAAA, ONERA, Institut Polytechnique de Paris, 92190 Meudon, France, selwyn.van der laan@onera.fr

<sup>&</sup>lt;sup>2</sup> DAAA, ONERA, Institut Polytechnique de Paris, 92190 Meudon, France

<sup>&</sup>lt;sup>3</sup>CEA-CESTA, 15 Avenue des Sablières, 33116, Le Barp, France

<sup>&</sup>lt;sup>4</sup>DAAA, ONERA, Institut Polytechnique de Paris, 92320 Châtillon, France

<sup>&</sup>lt;sup>5</sup> DAAA, ONERA, Institut Polytechnique de Paris, 91120 Palaiseau, France

weight and reducing performance or insufficient protection, risking failure and mission loss. Beyond heating, transition also affects aerodynamic performance by altering shock-boundary layer interactions (SBLI) near control surfaces, which can significantly modify wall pressure and heat loads [2], impacting stability, trajectory control, and structural integrity.

To investigate these mechanisms, this study considers the Cone-Cylinder-Flare (CCF) geometry introduced by Esquieu in 2020 [3], widely used in experimental [4, 5] and numerical [6, 7] work due to its ability to sustain diverse instability types. On the cone, both the first and second Mack modes are amplified, with the second mode dominating at Mach numbers above 4.5 [8, 9]. At the cone-cylinder junction, expansion damps the second mode, but downstream on the cylinder, the boundary layer may undergo separation, forming a recirculation bubble that may support global instabilities. These modes, sensitive to the flare angle, can couple with shear-layer instabilities, amplifying the first mode in the separated region while the second is damped [10]. After reattachment, the second mode regains dominance and grows strongly along the flare [4].

This study focuses on the role of wall temperature in transition, using the wall-to-recovery temperature ratio  $\frac{T_w}{T_r}$  as a control parameter. Here,  $T_r$  denotes the adiabatic wall temperature, and the ratio reflects the level of wall cooling. Prior studies have shown that reducing  $\frac{T_w}{T_r}$  destabilizes the second Mack mode while stabilizing the first [11, 12]. Most of these works assume uniform wall temperature, though recent research has demonstrated the potential of localized heating or cooling to selectively suppress instabilities [13, 14]. In practice, however, wind tunnels rarely reproduce flight-like thermal conditions because generating high-enthalpy flows is technically difficult. Facilities usually match Mach and Reynolds numbers but neglect thermal similarity, leading to discrepancies in boundary-layer evolution and transition onset. To address this, we perform numerical investigations combining global stability and resolvent analyses for three cases: (1) a reference wind tunnel condition, (2) a corresponding flight condition at the same Mach and Reynolds numbers but with realistic  $\frac{T_w}{T_r}$ , and (3) a "cold wall" case, where strong wall cooling in the tunnel reproduces the flight  $\frac{T_w}{T_r}$ . The aim is to assess whether including this additional similarity parameter enables ground-based experiments to better replicate flight transition mechanisms.

#### **Numerical framework**

## 2.1. CFD Solver

The computation of the baseflows and the extraction of the direct operator required for the stability analysis are performed using BROADCAST [15], an open-source solver developed by ONERA. This code employs a 7th-order reconstruction of the convective fluxes using a Flux-Extrapolated MUSCL scheme [16] and a five-point compact stencil for the computation of viscous fluxes. As we are studying the stability of hypersonic boundary layers in axisymmetric conditions, the flow is governed by the compressible Navier-Stokes equations in its conservative form:

$$\frac{\partial \mathbf{q}}{\partial t} = \mathcal{N}(\mathbf{q}) \tag{1}$$

where  $\mathcal{N}$  is the discretized Navier-Stokes operator and  $\mathbf{q} = (\rho, \rho u_x, \rho u_r, \rho u_\theta, \rho E)^T$  is the state vector in cylindrical coordinates. To study the linear dynamics, a 3D disturbance  $\mathbf{q}'$  is added to the baseflow  $\overline{\mathbf{q}}$ , a steady solution of the Navier-Stokes equation (i.e.  $\mathcal{N}(\overline{\mathbf{q}}) = 0$ ). This perturbation is such that  $\mathbf{q} = \overline{\mathbf{q}} + \mathbf{q}'$ ,  $||\mathbf{q}'|| \ll ||\mathbf{\bar{q}}||$  allowing to linearize the non-linear Navier-Stokes equations around the baseflow:

$$\frac{\partial \mathbf{q'}}{\partial t} = \mathcal{J}\mathbf{q'} \tag{2}$$

Eq. 2 is obtained with a Taylor expansion of the term  $\mathcal{N}(\overline{\mathbf{q}} + \mathbf{q}')$  and neglecting the terms smaller than  $o(\mathbf{q}')$ .  $\mathcal{J}$  is called the Jacobian of the flow and its expression is the following:

$$\mathcal{J} = \frac{\partial \mathcal{N}(\mathbf{q})}{\partial \mathbf{q}} |_{\overline{\mathbf{q}}} \tag{3}$$

As explained in the upcoming sections, the discrete jacobian  $\mathcal J$  is mandatory for the stability analysis, it is therefore computed via algorithmic differentiation using the software TAPENADE [17]. Furthermore, a so called 2.5D jacobian is computed where the  $\theta$ -direction components are computed analytically,

HiSST-2025-0086 Page | 2 Copyright © 2025 by the authors this allows the extension of the stability analysis to a 3D flow. The flow is first initialized with "implicit iterations" using the LU-SGS (Lower-Upper Symmetric Gauss-Seidel [18]) method. After the residuals have decreased by several orders of magnitude, we switch to a Newton method coupled with a pseudo-transient continuation approach [19]. Each state  $\mathbf{q}^n$  is updated using  $\mathbf{q}^{n+1} = \mathbf{q}^n + \delta \mathbf{q}^n$ , where  $\delta \mathbf{q}^n$  is computed the following way:

$$\left(\frac{I}{\Delta t} + \mathcal{J}(\mathbf{q}^n)\right) \delta \mathbf{q}^n = -\mathcal{N}(\mathbf{q}^n)$$
 (4)

## 2.2. Stability analysis

When dealing with global linear stability, two types of instabilities exist, global modes and resolvent modes, as shown in Figure

#### 2.2.1. Global analysis

As previously explained, global modes are self-sustained and intrinsic, meaning that no external forcing is needed. Only the self sustained dynamic of the flow is studied. As we consider an axisymmetric flow, a small disturbances can be expressed in a Fourier space by:

$$\mathbf{q}'(x, y, \theta, t) = \hat{\mathbf{q}}(x, y)e^{\lambda t + im\theta}$$
(5)

with  $\lambda = \sigma + i\omega$ ,  $\sigma$  the growth rate and  $\omega$  the pulsation. By injecting this in Eq. 2, the stability problem reduces to the following eigenvalue problem:

$$\mathcal{J}\hat{\mathbf{q}} = \lambda \hat{\mathbf{q}} \tag{6}$$

There is a global instability in the flow as soon as one eigenvalue has a positive real part ( $\sigma > 0$ ) meaning that the perturbation will grow exponentially in time. If there is no eigenvalue with a positive real part, the flow is globally stable.

Given that the modes are not orthognal with each other, even-though all eigenmodes are stable, convective instabilities may still exist thanks to the non-normality of the Navier-Stokes operator  $\mathcal{N}$  [20], the flow is then convectively unstable and some specific disturbances (noise-amplifier flow) will be convected and amplified downstream the flow. These modes are studied using resolvent analysis.

#### 2.2.2. Resolvent analysis

To accurately capture the convective modes, we have to focus on the response of the operator to an external forcing. Thus, we can add the forcing  $\mathbf{f}'$  to Eq. 2:

$$\frac{\partial \mathbf{q}'}{\partial t} = \mathcal{J}\mathbf{q}' + \mathbf{f}' \tag{7}$$

The external forcing  $\mathbf{f}'$  represents a noise source (naturally present in any real flow due to free-stream turbulence, sound waves ...). Considering Fourier modes :

$$\begin{cases} \mathbf{q}' = \hat{\mathbf{q}}(x, y)e^{i(m\theta + \omega t)} + c.c \\ \mathbf{f}' = \hat{\mathbf{f}}(x, y)e^{i(m\theta + \omega t)} + c.c \end{cases}$$
(8)

where c.c stands for complex conjugate. Note that q' and f' oscillate at the same frequency, as a forcing cannot induce a response at different frequencies within the realm of linear stability. Combining Eq. 7 & 8 we obtain the following equation:

$$\hat{\mathbf{q}} = \mathcal{R}(\omega, m)\hat{\mathbf{f}} \tag{9}$$

 $\mathcal{R}(\omega,m)=(i\omega\mathcal{I}-\mathcal{J}(m))^{-1}$  is called the resolvent operator, with  $\mathcal{I}$  being the identity matrix. This operator  $\mathcal{R}$  is a linear transer function between the forcing  $\mathbf{f}$  and the flow's response  $\mathbf{q}$ . For a given pulsation  $\omega$  and azimuthal wavenumber  $\theta$ , resolvent analysis aims to maximise the energy gain  $\mu^2$  between the forcing and the response:

$$\mu^2 = \frac{\|\hat{\mathbf{q}}\|_E^2}{\|\hat{\mathbf{f}}\|_E^2} \tag{10}$$

 $\|\cdot\|_E$  and  $\|\cdot\|_F$  denote the energy norms used to quantify the energy amplitude of the response and the forcing, respectively. In the spatially discretized framework, an inner product matrix can be defined such that:

$$\begin{cases} \|\hat{\mathbf{q}}\|_{E}^{2} = \langle \hat{\mathbf{q}}, \hat{\mathbf{q}} \rangle_{E} = \hat{\mathbf{q}}^{*} \mathcal{Q}_{E} \hat{\mathbf{q}} \\ \|\hat{\mathbf{f}}\|_{F}^{2} = \langle \hat{\mathbf{f}}, \hat{\mathbf{f}} \rangle_{F} = \hat{\mathbf{f}}^{*} \mathcal{Q}_{F} \hat{\mathbf{f}} \end{cases}$$
(11)

with  $\hat{\mathbf{q}}^*$  and  $\hat{\mathbf{f}}^*$  denoting the conjugate transpose of  $\hat{\mathbf{q}}$  and  $\hat{\mathbf{f}}$ . The choice of the energy matrices  $\mathcal{Q}_F$  and  $\mathcal{Q}_E$  in Eq. 11 is related to the energy of the perturbations that we wish to optimize. Chu's energy norm [21] is used here, it is the sum of kinetic energy and thermodynamic disturbances with the appropriate coefficients such that the conservative compression work is not included as a disturbance in the total energy [22].

Adding Eq. 11 into 10 and using 9 we obtain a Generalized Hermitian Eigenvalue Problem. The optimal forcing and the associated gain are then found by solving the following:

$$\mathcal{R}^* \mathcal{Q}_E \mathcal{R} \hat{\mathbf{f}}_i = \mu_i^2 \mathcal{Q}_F \hat{\mathbf{f}}_i \tag{12}$$

The highest eigenvalue  $\mu_0^2$  of Eq. 12 is the optimal gain, the corresponding eigenvector  $\hat{f}_0$  is the optimal forcing. The optimal response  $\hat{q}_0$  can then be computed using the resolvent operator, Eq. 9.

## 3. Baseflow Computation

#### 3.1. Geometry

The geometry selected to investigate the effects of wall temperature on boundary layer instabilities is the Cone-Cylinder-Flare with a 12 degree flare (CCF12) configuration. It begins with a spherical nose of 0.1 mm radius, followed by a cone with a 5° half-angle, which transitions into a 147 mm-long cylindrical section. Downstream of the cylinder is a 12° flare extending 105 mm. All associated geometric parameters are provided in Table 1. Additionally, due to its 0.1 mm nose radius and its 12° flare, this variant is classified as the "sharp" CCF12.

Parameter	<i>R<sub>n</sub></i> [mm]	L <sub>cone</sub> [mm]	L <sub>cyl</sub> [mm]	L <sub>flare</sub> [mm]	θ <sub>cone</sub> [°]	θ <sub>flare</sub> [°]
Value	0.1	398.2	147.3	104.9	5	12

**Table 1.** Geometrical parameters of the CCF12

Figure 1 illustrates the CCF12 geometry along with the key flow features. Initially, the flow passes over the cone, where a thin boundary layer of approximately 2 mm develops. As the flow reaches the cylinder, it encounters expansion waves that are due to the slope change between the cone and the cylinder. The 12° flare downstream of the cylinder generates an oblique shock at the compression corner, imposing a strong adverse pressure gradient (APG). If the boundary layer remains laminar, this APG causes boundary layer separation, forming a recirculation bubble (i.e. reversed and low-momentum flow) which is a favorable environment for the growth of global modes. The separated flow forms a shear layer above the recirculation bubble, which then reattaches to the flare surface, creating a reattachment shock completing the shock/boundary-layer interaction (SBLI) structure that governs the subsequent stability analysis.

#### 3.2. Flow conditions

The objective of this study is to examine how wall temperature influences transition mechanisms, based on the three flow conditions introduced in Section 1.. The reference, wind-tunnel conditions (R2Ch<sup>6</sup>) are taken from the literature: a Mach number of M=6 and a Reynolds number of  $Re=4.62\times10^6~\text{m}^{-1}$ 

<sup>&</sup>lt;sup>6</sup> ONERA Meudon's hypersonic wind-tunnel

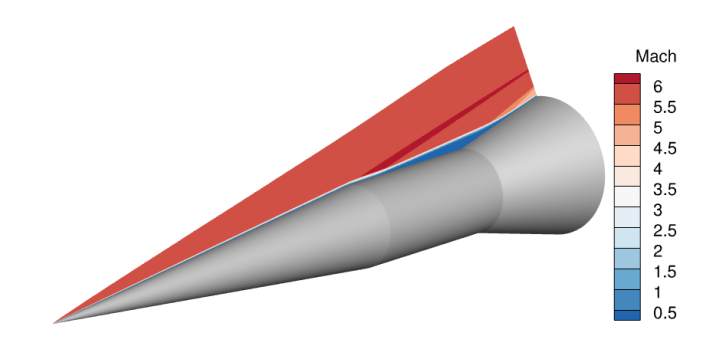


Fig 1. The CCF12 geometry with a Mach number field slice

, previously investigated both numerically by Caillaud *et al.* [7] and experimentally in ONERA's R2Ch hypersonic wind tunnel by Benitez *et al.* [23].

The second case represents a flight scenario, derived from the 1993 ICAO standard atmosphere model to match the Mach number and unit Reynolds number of the R2Ch case. The wall temperature, assumed constant along the CCF geometry, was set to 450K based on observations from the HIFiRE-1 experiment [24]. Since the focus is on wall-to-recovery temperature effects, this ratio was computed and is reported in Table 2.

Finally, the "cold" conditions were defined to enable ground-based reproduction of the flight case. These preserve the same Mach number and Reynolds number while matching the wall-to-recovery temperature ratio. Considering the R2Ch stagnation temperature limit of 750K, the resulting wall temperature is 185K. Lowering the wall temperature is thus the most practical way to mimic the wall-to-recovery temperature ratio of flight conditions experimentally, since achieving actual hypersonic stagnation temperatures in ONERA facilities is not possible. All flow parameters are summarized in Table 2.

Case	$u_{\infty}$ [m.s <sup>-1</sup> ]	$\rho_{\infty}$ [kg.m <sup>-3</sup> ]	$T_{\infty}[K]$	$T_0[K]$	$T_{W}[K]$	$T_{W}/T_{r}$ [-]	P <sub>0</sub> [kPa]
R2Ch	990.41	0.02128	67.80	555.96	300	0.597	653.94
Flight	1792.13	0.03735	222.00	1820.38	450	0.274	3758.26
Cold	1150.32	0.02534	91.46	750.00	185	0.274	1050.50

**Table 2.** Flow conditions considering M = 6, 0 & Re = 4,  $614 \times 10^6 \text{ [m}^{-1]}$ 

#### 3.3. Meshes

All three cases were computed on 2D axisymmetric meshes, which differ slightly due to variations in shock position and recirculation bubble size. The number of streamwise cells also changes, since at least 12 cells per wavelength are required to accurately capture the second Mack mode, as specified by Poulain *et al.* [15]. For global stability analyses, coarser meshes are sufficient because the recirculation bubble does not demand as much streamwise refinement. The mesh sizes used in this work are summarized in Table 3.

Case	Resolvent analysis	Cells / λ	Global stability
R2Ch	3500x550	16	3000x550
Flight	4040x550	13	3000x550
Cold	4100x550	13	3000x550

**Table 3.** Mesh sizes  $(N_X \times N_V)$ 

## 4. Numerical analysis of boundary layer instabilities in wind tunnel conditions

This section presents the stability analysis of the reference "R2Ch" case (Table 2), previously studied numerically by Caillaud [7] and experimentally by Benitez [23]. A brief overview of the main instabilities is provided to establish a baseline for examining wall-to-recovery temperature effects in the next section.

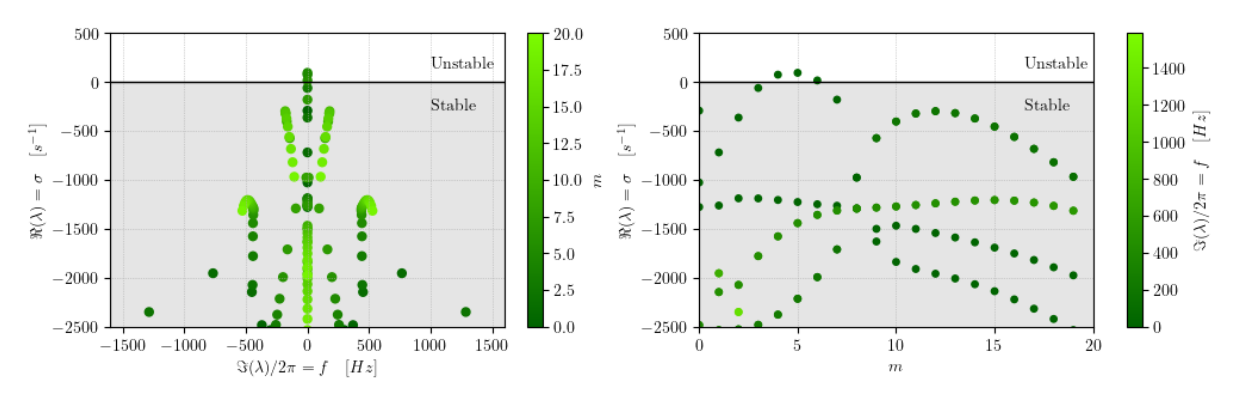


**Fig 2.** Eigenvalue spectrum. On the left, the eigenvalues plotted in the complex plane (growthrate  $\sigma$  and frequency f). The right plot shows the spectra in a growthrate-azimuthal wavenumber m plane.

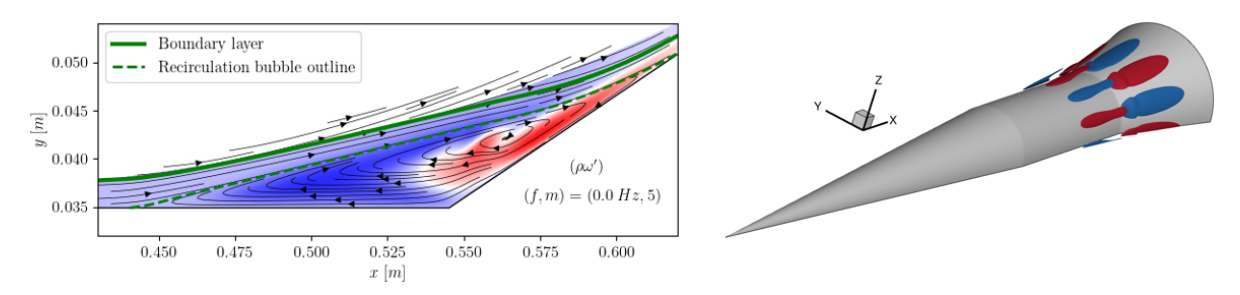


**Fig 3.** Leading global mode. The left image shows the most unstable global mode in a 2D version with the baseflow streamlines while the right plot is a 3D visual of the leading mode.

## 4.1. Global stability

Following the methodology explained in section 2.2.1., the eigenvalue spectra shown in Figure 2 is found. The left plot, showing the spectra in the complex plane demonstrates that there are multiple unstable modes at f = 0 [Hz]. The right plot adds that the most unstable eigenvalue is found for  $(f, m) = (0 \ Hz, 5)$ . Figure 3 shows the most unstable mode, note that the plot on the left is scaled. It is a 3D bubble mode whose amplitude fills the entire recirculation area. These 3D modes may lead to a three-dimensional flow upon which the convective instabilities may develop, Furthermore, these spectra are consistent with the results from [7].

#### 4.2. Resolvent Analysis

Although the flow exhibits a global instability that may alter its topology, we focus here on convective instabilities. Past experiments showed these to be dominant [23], with no evidence of global mode dynamics. Therefore, the resolvent analysis (Section 2.2.2.) is performed directly on the globally unstable flow.

Figure 4 shows the optimal gain map for the "R2Ch" case, where three regions of strong amplification can be identified. The first, around  $(f, m) = (180 \, kHz, 0)$ , corresponds to the second Mack mode—a 2D acoustic instability caused by waves trapped within the boundary layer below the sonic line. Its presence was confirmed experimentally by Benitez *et al.* [23] through high-frequency pressure transducer (PCB) measurements in both the R2Ch facility and the AFRL M6LT.

The right plot of Figure 4 shows the streamwise energy distribution of the optimal response (integrated along wall-normal lines). The second mode is strongly amplified over the cone, damped by the expansion fan and recirculation bubble, and then re-amplified after flow reattachment on the flare. The second region, around (f, m) = (50 kHz, 20), corresponds to the first Mack mode. With nonzero azimuthal wavenumber and frequency, it is a 3D instability driven by a generalized inflection point in the boundary layer. The Chu energy plot (Figure 4) indicates a different amplification mechanism from the second mode, as neither the expansion waves nor the recirculation bubble significantly affect its growth. Lugrin *et al.* [25] further showed that the first mode is amplified in the shear layer, but only at lower frequencies. Finally, the most amplified region, around (f, m) = (0 kHz, 60), corresponds to streamwise vortical

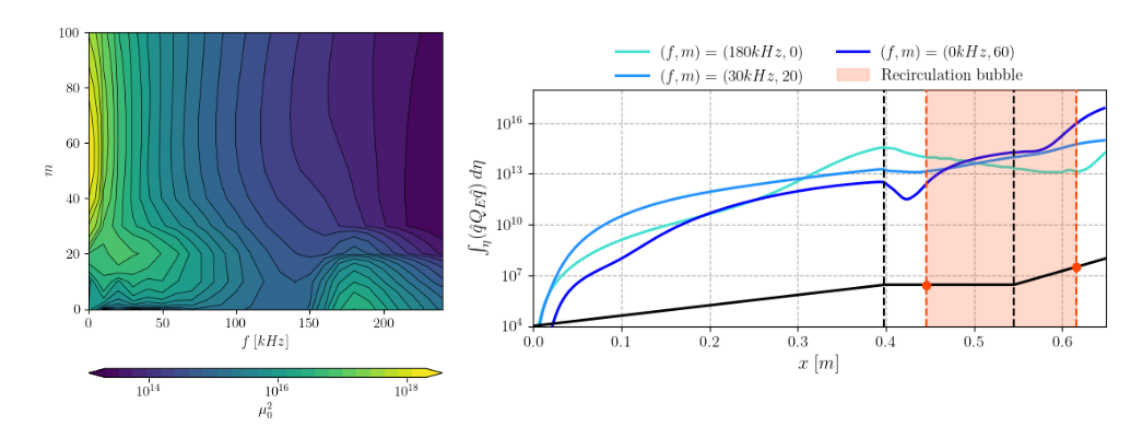


**Fig 4.** Left: Optimal gainmap in a frequency f and azimuthal wavenumber m space. Right: streamwise distribution of Chu's energy [21] of the optimal response for the three most amplified regions

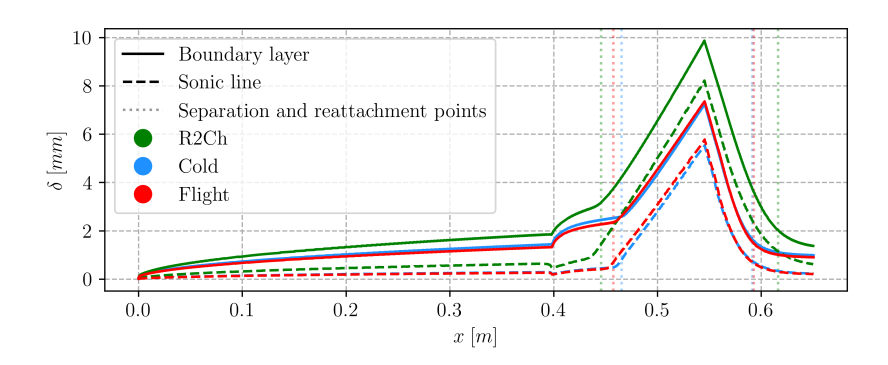


Fig 5. Boundary layer thickness, sonic line and separation positions comparison for the three baseflows

structures, hereafter referred to as streaks. These streaks are influenced by the expansion waves but are further amplified within the recirculation region, as discussed in the next section. A summary of all convective instabilities is provided in Table 4.

Instability	Frequency f [kHz]	Wavenumber m
First Mack mode	50	20
Second Mack mode	180	0
Streaks	0	60

**Table 4.** Summary of convective instabilities developing on the CCF in the wind tunnel conditions

## 5. Wall to recovery temperature ratio effects

We now examine the impact of flight conditions, along with the cold case, to assess whether they can be reproduced in a conventional wind tunnel by matching the wall-to-recovery temperature ratio. For clarity, results are color-coded: red for flight conditions, blue for cold conditions, and green for the wind tunnel case. We begin with baseflow comparisons, followed by an analysis of stability differences.

#### 5.1. Baseflow comparison

Figure 5 shows the streamwise evolution of the boundary-layer thickness  $\delta$ , computed from the total enthalpy  $h_{t,\infty}$ . With  $\eta$  denoting the wall-normal coordinate,  $\delta$  is defined using the criterion:

$$h_t(\eta = \delta) = 0.99 \times h_{t,\infty} \tag{13}$$

where  $h_{t,\infty}$  represents the freestream total enthalpy. The boundary layer first develops conventionally along the cone before accelerating under the expansion fan. It thickens further in the recirculation zone, reaching a maximum near the cylinder–flare junction, and then decreases after reattachment to values

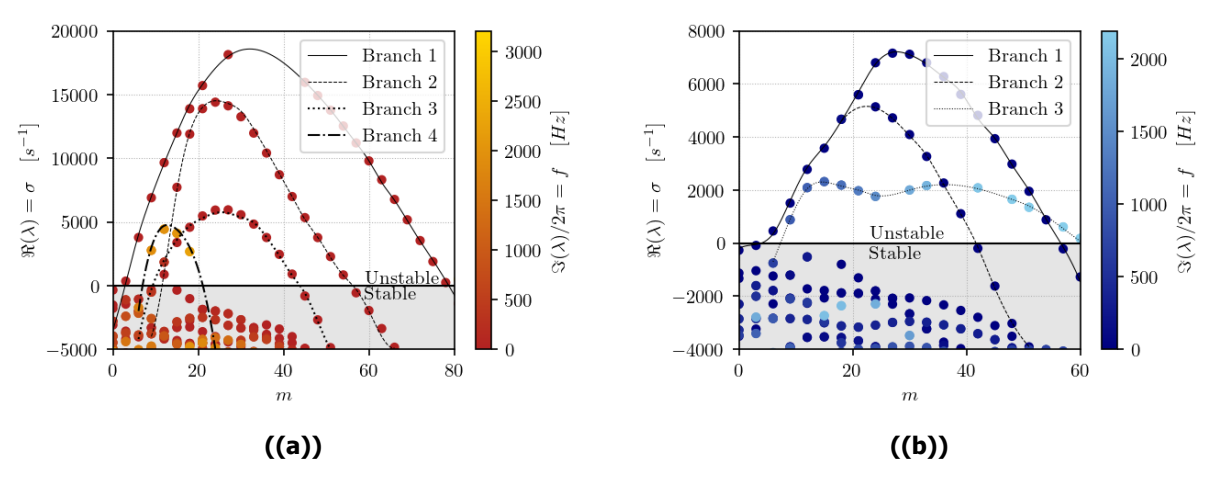


**Fig 6.** Global stability eigenvalue spectrum plotted in a growthrate  $\sigma$  and azimuthal wavenumber m space: (a) Flight conditions, (b) Cold case

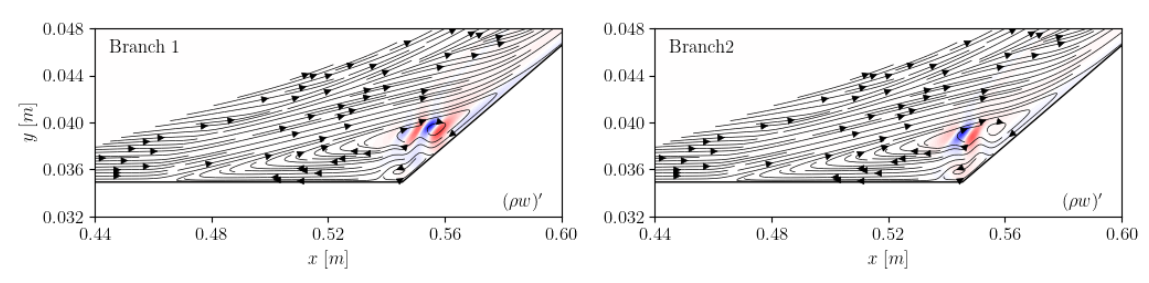


Fig 7. Leading global modes for branch 1 (Left) and branch 2 (Right) in the cold case

comparable with those at the cone's end. As expected, the flight case differs from the R2Ch wind tunnel case, showing a consistently thinner boundary layer across the geometry, consistent with [26], which highlights that matching only Reynolds and Mach numbers is insufficient to reproduce flight conditions in ground facilities. In contrast, the flight and cold cases agree well, suggesting similar boundary-layer stability behavior. Separation and reattachment points were identified as the first and last streamwise locations with negative velocity u. The resulting separation lengths are about 17.1 cm for R2Ch, 13.4 cm for the flight case, and 12.6 cm for the cold case. This reduction with decreasing wall-to-recovery temperature ratio aligns with [27] and has important implications for stability analysis, as changes in gradients directly affect the Jacobian.

## 5.2. Global stability

Figure 6 shows the global stability spectra for the flight and cold cases. Both exhibit more unstable modes than the R2Ch case (Figure 2), with multiple unstable branches at f=0~kHz and additional unsteady branches of lower growth rates. The nested recirculations in their separated regions promote extra global modes, each branch corresponding to a 3D mode in one of the recirculation cores (see Figure 7, where the leading modes of the cold case are plotted). The same behaviour occurs for the flight case. As in R2Ch, these modes are 3D, producing a three-dimensional recirculation bubble. The large growth rates  $\sigma$  suggest that both configurations bifurcate toward instability at lower Reynolds numbers than the wind tunnel case, which transitions at about  $Re=2.5\times10^6~[{\rm m}^{-1}]$  [7].

Although these global modes are strongly unstable, they are unlikely to directly trigger transition due to scale separation: low-frequency, low-wavenumber global modes mainly affect the recirculation region, whereas transition is driven by convective instabilities [25]. Furthermore, quiet wind-tunnel tests (flight-like conditions) [23] showed no evidence of global modes. Confirming this would require DNS studies, which lie beyond the scope of this work. Nevertheless, global modes may still indirectly influence transition by modifying the baseflow on which convective instabilities develop [28]. This justifies the use of resolvent analysis.

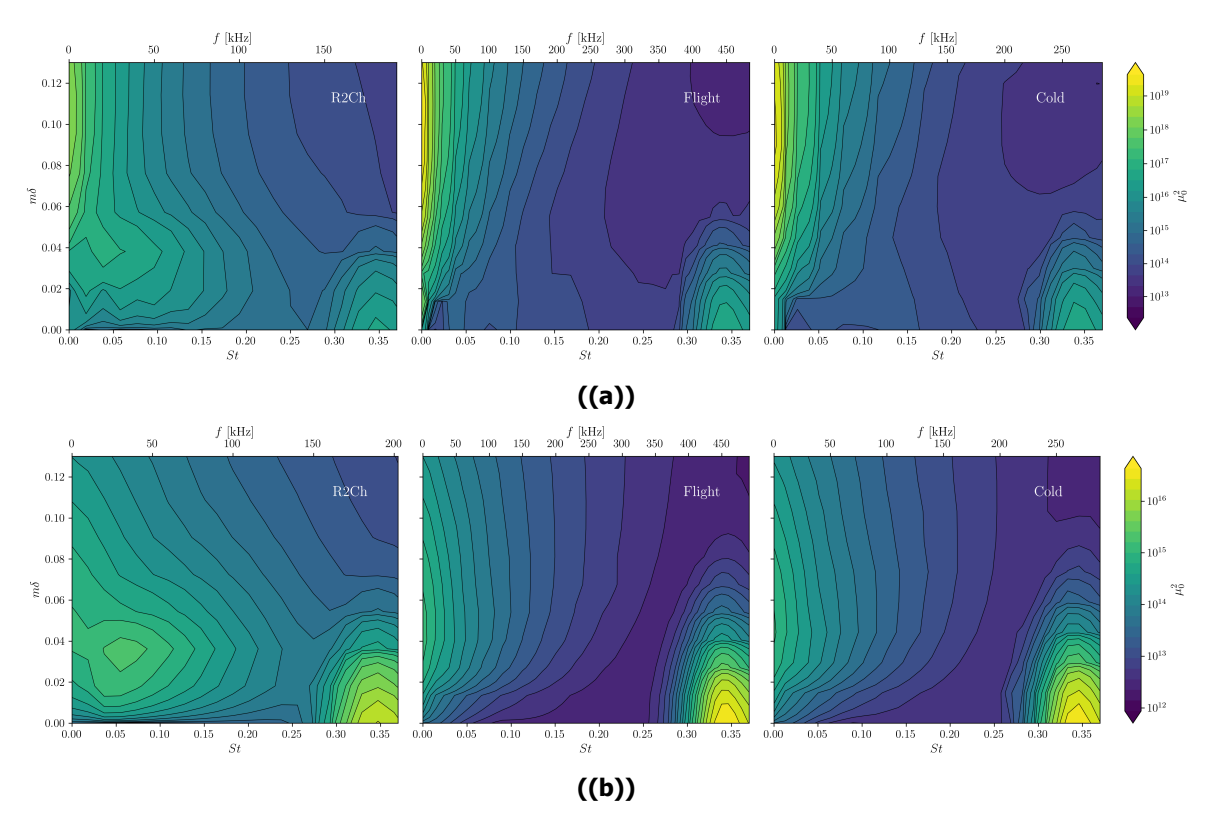


**Fig 8.** Optimal gainmap in a Strouhal St and azimuthal wavenumber times boundary layer thickness (taken at the end of the cone)  $m\delta$  space for the R2Ch - flight and cold cases: (a) Full CCF geometry, (b) Cone only

## 5.3. Resolvent Analysis

Figure 8 presents the optimal gain maps for all flow conditions. To enable consistent comparison, the maps are plotted in terms of the Strouhal number St on the x-axis, defined using the boundary-layer edge velocity  $u_e$ , the frequency f, and the boundary-layer thickness  $\delta$  at the end of the cone:  $St = \frac{f\delta}{u_e}$ .

For the y-axis, results are plotted as a function of  $m\delta$ , where m is the azimuthal wavenumber, providing the most meaningful comparison. The upper plots correspond to the full CCF geometry, while the lower ones are computed on cone-only baseflows. To allow energy gain comparisons, the same color scale is used for all flow conditions within each configuration. In each case, the CCF and cone gain maps show consistent similarities. Key observations from Figure 8 are outlined in the following paragraphs.

#### 5.3.1. First Mack mode

The first Mack mode, an oblique instability, appears in the wind tunnel case around  $(St, m\delta) = (0.05, 0.04)$  for both the CCF and cone-only configurations. In contrast, the cone results for the cold and flight cases (Figure 8(b)) show no amplified region at this location, consistent with [12]. As an inflectional mode, the first Mack mode depends on the presence of an inflection point in the boundary layer. In incompressible flows, its development is governed by Rayleigh's theorem [29], later generalized to compressible flows by Lees and Lin [30]:

$$\left. \frac{\partial}{\partial \eta} \left( \frac{\overline{\rho} \partial \overline{u}}{\partial \eta} \right) \right|_{\Omega_{\alpha}} = 0 \tag{14}$$

Eq. 14 defines the generalized inflection point criterion, which states that inflectional instability requires the existence of a point  $\eta_g$  in the boundary layer for which Eq. 14 is cancelled. This was evaluated at the end of the cone and inside the recirculation bubble (Figure 9). No generalized inflection points are observed in the flight and cold cases at the cone end ( $x = 0.38 \ m$ ) or elsewhere along

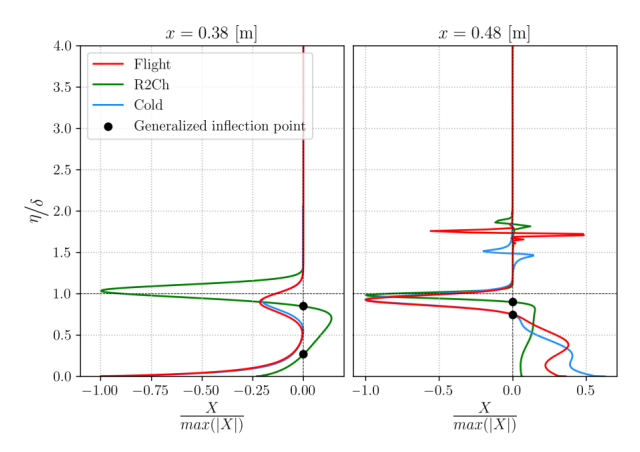


**Fig 9.** Generalized inflection point at two locations: Left - end of the cone, Right - middle of the cylinder (i.e. within the recirculation bubble)

the cone, explaining why the first mode is not amplified in these cases. In contrast, the R2Ch case does exhibit such points. The leftward shift of the curves for the flight and cold cases is linked to their lower wall-to-recovery temperature ratios, consistent with [8] and [12], who showed that a ratio near 0.25 is sufficient to suppress generalized inflection points at M=6. The right plot of Figure 9 focuses on the recirculation bubble (x=0.48), where a generalized inflection point appears in all three cases due to flow reversal. This explains the small energy peaks around ( $St, m\delta$ ) = (0.05, 0.04) in the flight and cold cases (Figure 8(a)). Since the inflection point only arises at separation, the first mode is amplified only downstream, leading to weaker energy growth. Finally, fluctuations observed for  $\frac{\eta}{\delta} \in [1.5, 2]$  are attributed to expansion waves from the cone–cylinder junction and do not affect the physical interpretation.

#### 5.3.2. Second Mack mode

For the second Mack mode, all cases exhibit a peak near  $(St, m\delta) = (0.33 - 0.35, 0.0)$ . The corresponding frequencies, however, differ significantly: about 450 kHz in the flight case, 260 kHz in the cold case, and 180 kHz in the R2Ch case. These shifts result from thinner boundary layers, as the second-mode frequency scales with  $f \sim \frac{u_e}{2\delta}$  [31]. The cold and flight cases also show stronger destabilization, with higher optimal gains (Table 5), visible as more intense yellow regions in Figure 8. These trends are consistent with [26], [32], and [8].

Cases	R2Ch	Cold	Flight
$\left(\frac{\mu_0^2}{\mu_{0,R2Ch}^2}\right)_{CCF}$	1	1.59	1.63
$\left(\frac{\mu_0^2}{\mu_{0,R2Ch}^2}\right)_{Cone}$	1	2.46	2.48

**Table 5.** Second Mack mode energy peaks differences

## **5.3.3.** Streaks

The last region of interest on these gainmaps is the region at St=0 (i.e.  $f=0\ kHz$ ). This region consists of stationary streaks and these are the most amplified disturbance mechanism. Caillaud [7] has shown that this is not true any more for higher Reynolds numbers (in the R2Ch conditions), where the Mack modes then become the most amplified. Still in our case, their energy peak is approximatively one order of magnitude higher than the other mechanisms. Regarding the flight and cold case, they have higher energy peaks for the streaks compared to the R2Ch case. This could be explained by centrifugal or baroclinic effects [33].

#### 6. Conclusion

This study investigated the influence of wall-to-recovery temperature ratio on hypersonic boundary-layer transition over the CCF geometry at Mach 6 by studying three cases: wind-tunnel (R2Ch), flight and a wall cooled (cold) case. Global stability and resolvent analyses revealed that flight and cold cases, unlike the wind-tunnel case, exhibit thinner boundary layers, more unstable bubble modes, and stronger second-mode amplification, while the first mode is suppressed due to the absence of generalized inflection points. The cold case successfully reproduced flight-like linear instability behaviour, showing that Mach and Reynolds similarity alone is insufficient to reproduce flight transition mechanisms. Incorporating wall-to-recovery temperature similarity is therefore essential for accurate replication of flight transition mechanisms in ground-based facilities.

## References

- 1. Hamilton, H. H., Millman, D. R. & Greendyke, R. B. Finite-Difference Solution for Laminar or Turbulent Boundary Layer Flow Over Axisymmetric Bodies With Ideal Gas, CF4, or Equilibrium Air Chemistry. NASA Technical Paper 3271 (1992).
- 2. Becker, J. V. & Korycinski, P. F. Heat Transfer and Pressure Distribution at a Mach Number of 6.8 on Bodies With Conical Flares and Extensive Flow Separation. NACA Research Memorandum L56F22 (1956).
- 3. Esquieu, S., Benitez, E. K., Schneider, S. P. & Brazier, J. P. Flow and Stability Analysis of a Hypersonic Boundary Layer Over an Axisymmetric Cone Cylinder Flare Configuration. AIAA SciTech Forum (2019).
- 4. Benitez, E., Esquieu, S., Jewell, J. & Schneider, S. Instability Measurements on an Axisymmetric Separation Bubble at Mach 6. AIAA AVIATION 2020 FORUM (2020).
- 5. Benitez, E. et al. Measurements on a Blunt Cone-Cylinder-Flare at Mach 6. AIAA SCITECH 2023 Forum (2023).
- 6. Paredes, P. et al. Boundary-Layer Instabilities over a Cone—Cylinder—Flare Model at Mach 6. AIAA Journal 60 (2022).
- 7. Caillaud, C. et al. Separation and Transition on a Cone-Cylinder-Flare: Computational Investigations. AIAA Journal, 497 (2025).
- 8. Mack, M. Boundary-Layer Linear Stability Theory. Jet Propulsion Laboratory, California Institute of Technology, AGARD Report No. 709 Part 3 (1984).
- 9. Group, N. S. A.-2. T. Hypersonic Boundary-Layer Transition Prediction. STO Technical Report, AC/323(AVT-240)TP/902 (2020).
- 10. Caillaud, C., Lugrin, M., Esquieu, S. & Content, C. Global Stability Analysis of a Hypersonic Cone-Cylinder-Flare Geometry. 57th 3AF International Conference on Applied Aerodynamics AERO 2023 (2023).
- 11. Liang, X., Li, X., Fu, D. & Ma, Y. Effects of wall temperature on boundary layer stability over a blunt cone at Mach 7.99. Computers & Fluids 39, 359–371 (2010).
- 12. Masad, J., Nayfeh, A. & Al-Maaitah, A. Effect of heat transfer on the stability of compressible boundary layers. Computers & Fluids 21, 43–61 (1992).
- 13. Bilto, M., Liang, T., Kafle, S. & Kuehl, J. J. Numerical Investigation of Wall Temperature Effects on Hypersonic Modal Flow Instabilities in Double Cone and Cone-Cylinder Flare Separation Bubble. AIAA SCITECH 2025 Forum (2025).
- 14. Poulain, A., Content, C., Rigas, G., Garnier, E. & Sipp, D. Adjoint-based linear sensitivity of a supersonic boundary layer to steady wall blowing—suction/heating—cooling. Journal of Fluid Mechanics 978, A16 (2024).
- 15. Poulain, A., Content, C., Sipp, D., Rigas, G. & Garnier, E. BROADCAST: A High-Order Compressible CFD Toolbox for Stability and Sensitivity Using Algorithmic Differentiation. Computer Physics Communications 283 (2023).
- 16. Cinnella, P. & Content, C. High-order implicit residual smoothing time scheme for direct and large eddy simulations of compressible flows. Journal of Computational Physics 326, 1–29 (2016).

- 17. Hascoet, L. & Pascual, V. The tapenade automatic differentiation tool: principles, model, and specification. ACM Transactions on Mathematical Software (TOMS) 39, 1–43 (2013).
- 18. Yoon, S. & Jameson, S. A Multigrid LU-SSOR Scheme for Approximate Newton Iteration Applied to the Euler Equation. NASA CR-179524 (1986).
- 19. Crivellini, A. & Bassi, F. An Implicit Matrix-Free Discontinuous Galerkin Solver for Viscous and Turbulent Aerodynamic Simulations. Acta Mechanica 1, 215–234 (1965).
- 20. Schmid, P. J. Nonmodal Stability Theory. Annual Review of Fluid Mechanics 39, 129–162 (2007).
- 21. Chu, B. On the Energy Transfer to Small Disturbances in Fluid Flow (Part 1). Acta Mechanica 1, 215–234 (1965).
- 22. A. Hanifi P. Schmid, D. Transient growth in compressible boundary laver flow. Physics of Fluids 8 (1996).
- 23. Benitez, E. K. et al. Separation and Transition on a Cone-Cylinder-Flare: Experimental Campaigns. AIAA SciTech Forum (2024).
- 24. Li, F. et al. Transition Analysis for the Ascent Phase of HIFiRE-1 Flight Experiment. Journal of Spacecraft and Rockets 52, 1273–1519 (2015).
- 25. Lugrin, M., Beneddine, S., Leclerq, C., Garnier, E. & Reynald, B. Transition scenario in hypersonic axisymmetrical compression ramp flow. Journal of Fluid Mechanics 907 (2021).
- 26. Hader, C. & Fasel, H. F. Numerical Investigation of the Laminar-Turbulent Boundary-Layer Transition for a Circular Cone at Mach 5: Wind Tunnel and Flight Conditions. AIAA SciTech Forum (2023).
- 27. Zhang, D., Yuan, X., Liu, S., Zhu, K. & Liu, W. Experimental study of wall temperature effect on shock wave/turbulent boundary layer interaction in hypersonic aircraft. Energy 263, 125753 (2023).
- 28. Lugrin, M., Beneddine, S., Garnier, E. & Reynald, B. Multi-scale study of the transitional shock-wave boundary layer interaction in hypersonic flow. Theoretical and Computational Fluid Dynamics 36, 277–302 (2022).
- 29. Rayleigh, L. On the Stability, or Instability, of Certain Fluid Motions. London Mathematical Society 1, 57–72 (1879).
- 30. Lees, L. & Lin, C. Investigation of the Stability of the Laminar Boundary Layer. NACA Technical Note 1115 (1946).
- 31. Demetriades, A. Pressure Fluctuations on Hypersonic Vehicles Due to Boundary-Layer Instabilities. AIAA Journal 24 (1986).
- 32. Knisely, C. P. & Zhong, X. Significant Supersonic Modes and the Wall Temperature Effect in Hypersonic Boundary Layers. AIAA Journal 57, 1552–1566 (2019).
- 33. Dwivedi, A., Sidharth, G. S., Nichols, J. W., Candler, G. V. & Jovanovic, M. R. Reattachment Streaks in Hypersonic Compression Ramp Flow: An Input-Output Analysis. Journal of Fluid Mechanics 880, 113–135 (2019).